Iranian Journal of Geophysics, Vol 16 No 4, 2023, Page 1 – 18 (Research Article)
DOI: 10.30499/ijg.2022.346697.1433

Application of two-step GIT on source, path and site effects case study: Mw7.3 Sarpol-e Zahab great earthquake on 12 November 2017

Seyed Reza Sakhaei [1], Majid Mahood [2*], Reza Heidari [3] and Mehran Arian [4]

[1] *PhD student, Department of Earth Sciences, Science and Research Branch, Islamic Azad University, Tehran, Iran*
[2] *Assistant Professor, International Institute of Earthquake Engineering and Seismology (IIEES), Tehran, Iran*
[3] *Assistant Professor, Department of Earth Sciences, Science and Research Branch, Islamic Azad University, Tehran, Iran*
[4] *Associate Professor, Department of Earth Sciences, Science and Research Branch, Islamic Azad University, Tehran, Iran*

(Received: 11 June 2022, Accepted: 21 August 2022)

Abstract

One of the largest earthquakes in the Zagros region occurred on November 12, 2017, in Sarpol-e Zahab with Mw=7.3. We considered the aftershocks of this event and collected the S-wave amplitude spectra from 87 strong-motion records to determine the source, path, and site effects using a non-parametric generalized inversion technique. The grid-searching method based on Brune's ω_2 model was employed to determine some of the source parameters. The corner frequency and seismic moment vary from 1.11 to 5.14 *Hz* and from 9.12×10^{14} to 1.36×10^{17} N.m, respectively. Also, The seismic moment and the cube of corner frequency are inversely related to each other. The stress drop of earthquakes is determined with the ε indicator. In this study ε is equal to 1.91; thus this value indicates that frictional overshoot has occurred with the dynamic frictional stress larger than the final stress. The S-wave quality factor is estimated as Q=101f0.67. The value of Q_0 is small, which is characteristic of an active tectonic environment. We compared the site effects that were calculated by GIT and H/V methods. In most cases, a very good agreement was observed and the small difference between them is mainly due to the constraints and assumptions of these methods.

Keywords: Attenuation function, generalized inversion, site effect, source parameters, Zagros

*Corresponding author: m.mahood@iiees.ac.ir

1 Introduction

The convergence between the Arabian plate in the southwest and Eurasia in the northeast led to the formation of the Zagros continental collision zone (Jackson and McKenzie, 1984). The Zagros is an active area and most of its events have magnitude less than 5.0 and only one events with M>7.0 within 400 years. The Zagros region is affected by frequent earthquakes of magnitude generally less than 5 at the depth of lower than 20 Km beneath the sedimentary sequence (Paul et al., 2006). No earthquake with a depth of more than 30 km has occurred in the Zagros (e.g. Tatar et al., 2004; Nissen et al., 2011), attesting that subduction is not seismically active beneath the suture at present (Motaghi et al., 2017). One of the largest earthquakes in the region occurred on November 12, 2017, in Sarpol-e Zahab (near the Iranian-Iraqi border). The lat., long., Depth, and O.T. are reported as 34.77 ˚N, 45.76 ˚E, 18 km, and 18:18:16, respectively. Several studies have been conducted on the parameters of source, attenuation, and site effect for different regions of Iran. The results of this research can be used in the estimation of region-specific parameters to predict accurate ground-motion amplitudes, simulating strong ground motion and studies seismic hazard analysis. For example, recently Ahmadzadeh et al. (2017) estimated the site and the source parameters for the 2006 Silakhor aftershocks using the generalized inversion approach. Sakhaei et al. (2021) also used the same approach to determine the parameters of Sarpol-e Zahab region.

The purpose of this paper is to estimate source parameters, path attenuation, and site effects. To achieve this goal, a 2-step generalized inversion technique was used. This method was first proposed by Andrews (1986) by recasting the method of spectral ratios into a generalized inverse problem. Other researchers used and developed this method (e.g. Castro et al., 1990; Boatwright et al., 1991;Hartzell, 1992; Parolai et al., 2000; Salazar et al., 2007; Oth et al., 2008, 2009). Source spectra, attenuation characteristics, and site

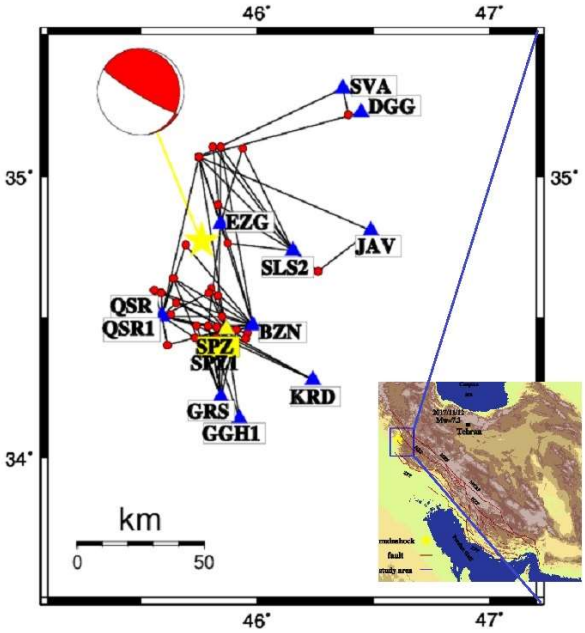

Figure 1. Magnified image of the blue box on the left; red circle: aftershocks, blue triangle: stations (the reference station is highlighted), black line: records ray path.

response functions were obtained using only as many constraints as necessary to be able to solve the inversion problem, and not assumed any predefined functional form of the source spectra or the attenuation. Appropriate aftershocks of Sarpol-e Zahab Mw=7.3 mainshock were selected from November 12, 2017, to January 18, 2018, and their S-wave spectra were extracted as inversion inputs (observed data). The source spectrum was adapted to Brune's model (1970, 1971) to estimate some of the source parameters such as corner frequency, seismic moment, radiated energy, etc. From the attenuation function, the quality factor and geometrical spreading were determined and compared with other previous studies in this area. Finally, the site effects were obtained and compared with the H/V method.

Table 1. The accelerometer stations were used in this study. Vs30 for the number of stations is reported by BHRC. The surface geology is based on the geological base map (1:250,000 scale) of the Geological Survey of Iran.

ID	Station Code	Number of Records	Longitude (°)	Latitude (°)	Elevation (m)	V_{s30} (m/s)	Type of Instrument	Geology Condition
1	GRS	9	45.845	34.218	663	403	SSA-2	Marl, limestone, and shale (Upper Cretaceous to Paleocene) Gurpi-Pabdeh Formation
2	SPZ	14	45.868	34.459	558	619	SSA-2	Thin-walled, fine-grained clay limestones, with shale and regular stratification
3	SPZ1	5	45.868	34.459	558	619	Guralp	Thin-walled, fine-grained clay limestones, with shale and regular stratification
4	BZN	15	45.982	34.473	1009	-	SSA-2	Dolomite, dolomitic limestone, limestone (Shahbazan- Asmari Formation)
5	KRD	3	46.240	34.279	1562	800	SSA-2	Dolomite, dolomitic limestone, limestone (Shahbazan- Asmari Formation)
6	QSR	11	45.591	34.506	395	340	SSA-2	Gypsum and evaporative sediments (Gachsaran Formation)
7	QSR1	7	45.591	34.506	395	340	Guralp	Gypsum and evaporative sediments (Gachsaran Formation)
8	DGG	2	46.447	35.226	1295	-	SSA-2	Sandy shale, limestone lenses and volcanics
9	SVA	2	46.369	35.311	1025	-	SSA-2	Massif and thick bedded partly fetid limestone (Mainly upper Jurassic)
10	EZG	8	45.843	34.832	710	-	SSA-2	Thin-walled, fine-grained clay limestones, with shale and regular stratification
11	SLS2	7	46.154	34.738	1248	281	SSA-2	Limestone containing radiolarite with pyrite and chert shale (Garau Formation)
12	GGH1	2	45.925	34.140	830	692	Guralp	Marl, limestone, and shale (Upper Cretaceous to Paleocene) Gurpi-Pabdeh Formation
13	JAV	2	46.489	34.809	1340	298	SSA-2	radiolarites, intercalated with radiolarian bearing marls and siliciferous

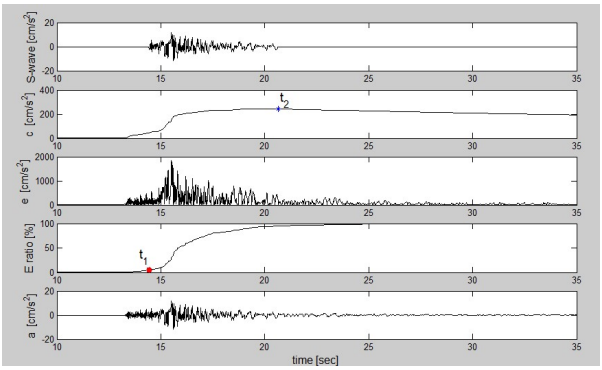

Figure 2. Demonstrating the approach used in this study for finding the start and end times of the S-wave (t_1 and t_2). From bottom to top: a corrected record by fourth-order Butterworth bandpass filter (0.1-30 Hz), Husid plot (Energy ratio E/E_t) to estimate start time (t_1), envelope function, cumulative function to estimate the end time (t_2), the S-wave record.

1 Data Processing

In order to perform inversion, the records of the accelerometer network of Road, Housing, and Urban Development Research Center of Iran have been used. The criteria for selecting the data were signal-to-noise ratio larger than 3, recording of each event by at least two stations, and recording of at least two events by each station. Based on these conditions, 87 records were selected from the available data (black line in Figure 1). These records, which were recorded in 13 stations (Table 1), are related to 30 aftershocks. The location, origin time, and magnitude of these aftershocks are listed in Table 2 by Sakhaei et al. (2021). Sampling rate and instrument period are 200 and 0.02 seconds, respectively. Most records were recorded by stations BZN and SPZ with 15 and 14 data, respectively. The origin time, location, and magnitude of the events are taken from the International Seismological Center (IRSC). The magnitude range of ML is from 3.8 to 5.3 and the hypocentral distance range is from 9 to 70 km. Of course, records with larger hypocentral distances were also available, but due to the low density of records at distances larger than 70 km, they were not selected for inversion.

Since the major portion of the seismic energy is generated in the form of S-waves, the analysis should be performed on this part of the strong motion records (Zafarani et al., 2012). Husid's (1967) method was used to select the start time of S wave (t_1); That is when the record energy (E) reaches 5% of the total wave energy (E_t). Kinoshita's (1994) method was also used to select the end time of the S-wave (t_2). Kinoshita (1994) defined the acceleration envelop function (e(n)) and the cumulative acceleration function (c(k)) according to the following equations:

$$e(n) = (a^2(n) + H^2\{a(n)\})^{1/2} \quad (1)$$

$$c(k) = (k^{-1} \sum_{n=1}^{k} e^2(n))^{1/2} \quad (2)$$

In this relationship, **a** is the record of acceleration and **H** is the Hilbert transform. In this method, the end time of the S-wave is equal to the time at which the cumulative envelope function begins to decline (Figure 2). In the next step, the Fourier spectrum of the S-wave must be calculated. However, the sudden interruption of the wave has a great impact on the Fourier spectrum. Therefore, after selecting the time of the beginning and end of the S-wave, a cosine taper was applied to it. In this study, the length of each taper was considered as 5% of the total length of the record.

The mentioned steps should be done for both horizontal components and then their root mean square (RMS) should be calculated. Due to sudden changes in the Fourier spectrum, a smoothing function must

be applied to it. One of the suitable methods for this work is the method of Konno and Ohmachi (1998). In this method, a window is applied to the records according to the following equation:

$$W(f, f_c) = \left[\frac{\sin(\log(\frac{f}{f_{cent}})^b)}{\log(\frac{f}{f_{cent}})^b}\right]^4 \quad (3)$$

where f_{cent} represents the center frequency around which the smoothing is performed, and b is a constant number where supposed b=40. The frequency range in this study is 0.5 to 25 Hz, from which the values of the acceleration spectrum at 40 points with the same logarithmic distances are interpolated from this range.

As mentioned, one of the criteria for choosing the appropriate record is that the signal-to-noise ratio is greater than 3 (SNR(f) >3). For this purpose, pre-event noise windows with the same length as the S-wave windows were selected and then their Fourier Amplitude Spectrum (FAS) was calculated. For example, the signals of two different events with their FAS are shown in Figure 3. SNR was calculated at 40 selected frequencies (in the range of 0.5 to 25 Hz) to test condition SNR(f) >3.

3 Two-Step Generalized Inversion Technique (GIT)

We have used the 2-step generalized inversion technique to estimate some seismic parameters. This method is based on the ground motion convolution model (multiplication in the frequency domain):

$$U_{ij}(f, R) = A(f, R_{ij}).S_i(f).G_j(f) \quad (4)$$

Where $U_{ij}(f, R)$ is the FAS (in this study, the horizontal component of the observed acceleration) from the i-th source and the j-th station at the hypocentral distance R. $S_i(f)$ is the source function and A(f, R) is the attenuation function along the path (e.g. geometrical spreading, anelastic and scattering attenuation) and Gj(f) is the local amplification of the site. We applied logarithms to both sides of this equation, to achieve a linear problem:

$$\log U_{ij}(f, R) = \log A(f, R) + \log S_i(f) + \log G_j(f) \quad (5)$$

Castro et al. (1990) proposed a 2-step GIT which does not include any parameterization of the attenuation characteristics. The advantage of the 2-step method is that by splitting the problem into subinversions, the number of unknowns involved for each of these cases becomes significantly smaller, which makes the inversion problem more practicable (Castro et al., 1995; Oth, 2007). In the first step, the observed spectra can be expressed as:

$$U_{ij}(f, R) = A(f, R_{ij}).M_i(f) \quad (6)$$

Where M is a scale factor for source i (dependent on the size of ith earthquake). There is no presumption about the form of the attenuation function, but it is constrained to be a smooth function of distance and its value is 1 in the reference distance (R_0). By taking the logarithm of Equation 6 and converting it to a linear problem, the system of equations can be written as the following matrix:

$$\begin{bmatrix} 1 & 0 & 0 & 0 & \cdots & 0 \\ 0 & 1 & 0 & 0 & \dots & 0 \\ \vdots & \vdots & \vdots & \vdots & \vdots & \vdots \\ 0 & 0 & 0 & 0 & \dots & 1 \\ \omega_1 & 0 & 0 & 0 & \cdots & 0 \\ -\omega_2/2 & \omega_2 & -\omega_2/2 & 0 & \cdots & 0 \\ 0 & -\omega_2/2 & \omega_2 & -\omega_2/2 & \cdots & 0 \\ \vdots & \vdots & \vdots & \vdots & \vdots & \vdots \end{bmatrix} \begin{bmatrix} 1 & 0 & \cdots & 0 \\ 0 & 1 & \cdots & 0 \\ \vdots & \vdots & \vdots & \vdots \\ 0 & 0 & \dots & 1 \\ 0 & 0 & \cdots & 0 \\ 0 & 0 & \cdots & 0 \\ 0 & 0 & \cdots & 0 \\ \vdots & \vdots & \vdots & \vdots \end{bmatrix}$$

$$\begin{bmatrix} \ln A(f, R_1) \\ \ln A(f, R_2) \\ \ln A(f, R_3) \\ \vdots \\ \ln A(f, R_N) \\ \ln M_1(f) \\ \ln M_2(f) \\ \vdots \\ \ln M_i(f) \end{bmatrix} = \begin{bmatrix} \ln U_1(f, R_1) \\ \ln U_2(f, R_2) \\ \vdots \\ \ln U_N(f, R_N) \\ 0 \\ 0 \\ 0 \\ \vdots \end{bmatrix} \quad (7)$$

Where ω_1 is a weighting factor to constrain A(f, R_0) = 1 at reference distance (R_0), and the value ω_2 determines the degree of smoothness of the solution by imposing a small second derivative concerning distance. The distance is divided into N parts and the attenuation function is calculated for each part.

In the second step, the attenuation function obtained in the first step is divided by

the observed record, and then another inversion is performed for the source spectrum and site effects:

$$\frac{U_{ij}(f,R_{ij})}{A(f,R_{ij})} = S_i(f).G_j(f) \quad (8)$$

In this step, there is a trade-off between the source and site functions. To eliminate this degree of freedom, the site amplification function for one or more stations can be considered a default value (Andrews, 1986).

Parolai et al. (2000, 2004) employed the Efron's (1979) bootstrap method to analyze the stability of inversion with new data set. In this study, we used
these methods and repeated inversion in 100 iterations. Then, the mean and standard deviation of each parameter is estimated.

4 Source parameters

It should be noted that in the first step of inversion, the cumulative attenuation within the reference distance does not appear in A(f, R), but manifests itself in the second step of inversion. Due to the elimination of the trade-off between the source and the site functions by selecting the default values for site amplification of one or more sites, the source functions will include cumulative attenuation effect. Therefore, its effect must be removed from the inverted source spectra. In other words, the source spectrum obtained in inversion (S_{inv}) must be divided into the cumulative attenuation (ψ) to obtain the real source spectrum (S):

$$S(f) = {S_{inv}(f)}\Big/{\psi(f)} \quad (9)$$

Assuming that the source spectrum follows the ω^2 source model (Brune, 1970; 1971):

$$S(f) = (2\pi f)^2.\frac{R_{\theta\phi}VF}{4\pi\rho_S\beta_S^3R_0}.\frac{M_0}{1+(f/f_c)^2} \quad (10)$$

Where $R_{\theta\phi}$ is the mean value of the radiation pattern of the S-wave and the value $V=1/\sqrt{2}$ is considered for the separation of S-wave energy on two horizontal components. F is the free surface amplification that is considered equal to 2 in most studies. β_s and ρ_s are the shear wave velocity and density near the source, respectively. M_0 and f_c are also seismic moment and corner frequency, respectively.

Where the unit of the seismic moment in this relationship is dyn-cm (10^{-7}N.m). If a small earthquake (Here with the S index) is regarded as the empirical Green's function (EGF) of a large earthquake (Here with the L index), the differences of the path attenuation in the strong-motion recordings at the same station from large and small earthquakes can be ignored. The FAS ratio $U_L(f)/U_S(f)$ can be approximately expressed as the theoretical source spectral ratio $S_L(f)/S_S(f)$ (Wang et al., 2018):

$$\frac{U_L(f)}{U_S(f)} \approx \frac{S_L(f)}{S_S(f)} = \frac{M_{0L}}{M_{0S}}.\frac{1+(f/f_{cS})^2}{1+(f/f_{cL})^2} \quad (11)$$

According to this relationship, the corner frequencies for the large and the small events can be obtained by minimizing the difference between the observed FAS ratio and the theoretical source spectrum ratio. By substituting the corner frequency in Equation 10, the theoretical source spectrum is obtained and then the cumulative attenuation ψ can be estimated by using Equation 9.

In this study, source number 30 was selected as a large earthquake, and sources number 9, 10, and 12 were selected as small earthquakes. The cumulative attenuation function was calculated with these three pairs of large/small earthquakes: 30/9, 30/10, and 30/12. The seismic moments of these 4 events were calculated with the relationship proposed by Nemati and Tatar (2015) as $\log M_0 = 1.47\,ML + 9.19$. The grid searching method was used to obtain the corner frequencies. The best adaptation between the spectral ratio of large to small sources (observational and theoretical) was obtained in the ratio of S30/S10 with RMS=0.46. Three small

earthquakes have three different magnitudes. However, the cumulative attenuation functions are independent of the magnitude of the selected earthquakes (Figure 4). In this study, an average of three ψ functions was taken to determine the final cumulative attenuation function.

In the next step, all source functions that were achieved from inversion were divided into ψ to obtain the real source functions. Then, the corner frequency and seismic moment corresponding to each source will be calculated by fitting the real source function and the Brune (1970, 1971) source model. For this purpose, the grid searching method has been used. For the range of the seismic moment variation, the equation proposed by Hanks and Kanamuri (1979) ($\log M_0 = 1.50\, M_w + 9.05$) and the condition of ML-0.40 ≤Mw≤ ML+0.40 are used. Since the stress drop Δσ for small to moderate earthquakes varies from 0.1 to 100 MPa (Kanamori, 1994), the range of corner frequency will be calculated according to the ranges of stress drop and seismic moment, and based on Brune's equation:

$$f_c = 4.9 \times 10^6 \beta \left(\Delta\sigma / M_0\right)^{1/3} \qquad (12)$$

For example, the 3 sources with their best-

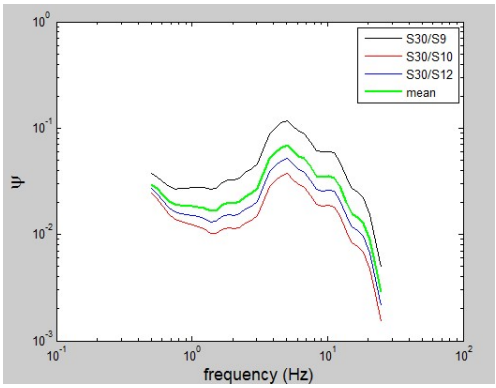

Figure 4. The cumulative attenuation function was obtained with three pairs of earthquakes and their average.

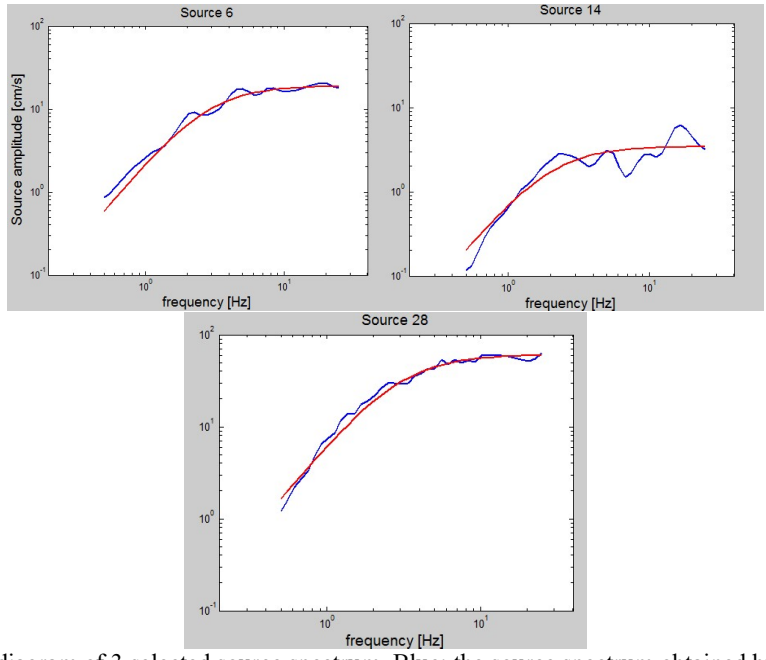

Figure 5. The diagram of 3 selected source spectrum. Blue: the source spectrum obtained by GIT. Red: the best-fitted curve (theoretical source).

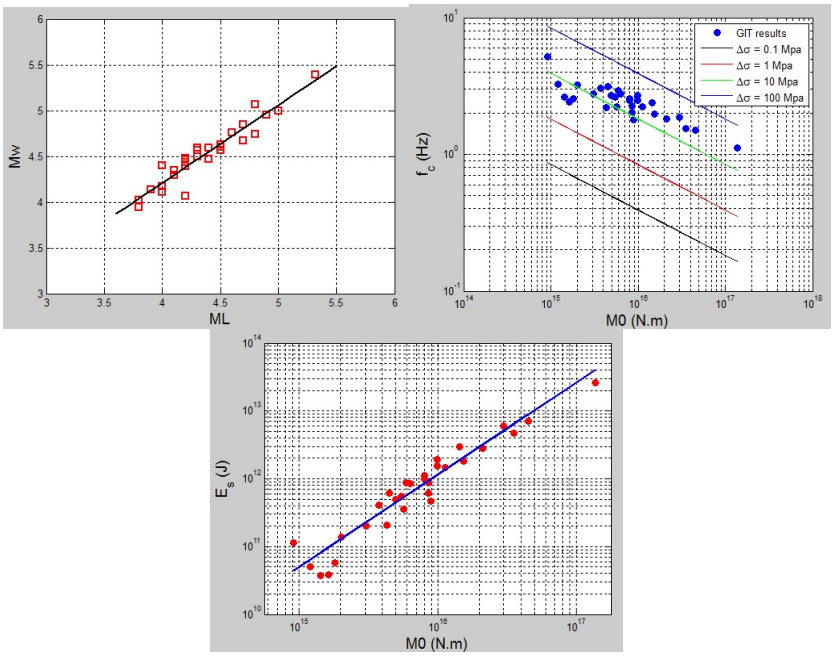

Figure 6. (Left) Moment magnitude (Mw) versus local magnitude (ML) with the best-fitted line Mw=0.86ML+0.76 (R^2=0.91), (middle) corner frequency versus seismic moment, (right) S-wave radiated energy versus seismic moment with the best-fitted line.

fitted theory curves are shown in Figure 5. The maximum and minimum values of the corner frequencies are 5.14 and 1.11 Hz, for sources 11 and 24, respectively. Also, the seismic moment varies from 9.12×10^{14} to 1.36×10^{17} N.m, with the maximum and minimum values being for sources 24 and 11, respectively (Table 2). The Mw range is obtained from 3.94 to 5.39. The best-fitted line for this diagram is estimated to be Mw=0.865 ML + 0.76 and its regression correlation coefficient was R^2=0.91. The diagram of Mw versus local magnitude (ML) is shown in Figure 6.

Other quantities such as the source radius r and the stress drop Δσ in Brune's model (Brun 1970, 1971) are defined as follows:

$$r = \frac{2.34\,\beta_s}{2\pi\,f_c} \qquad (13)$$

$$\Delta\sigma = \frac{7\,M_0}{16\,r^3} \qquad (14)$$

Also, the apparent stress σ_a can be calculated by $\sigma_a=\mu E_s/M_0$. where μ and E_s are the rigidity modulus ($\mu=\rho.\beta^2$) and the radiated energy of S-wave, respectively. In this study, the equation of Izutani and Kanamori (2001) is used to estimate the S-wave energy:

$$E_s = \frac{4\pi}{5\rho\beta^5}\int_0^\infty \left|\frac{f\,M_0}{1+(\frac{f}{f_c})^2}\right|^2 df \qquad (15)$$

All of these values mentioned above are listed in table 2. The maximum and minimum values of the stress drop are 33.37 and 3.84 MPa, respectively. The relationship between stress drop and apparent stress is estimated as $\Delta\sigma=4.52\sigma_a$. The range of S-wave radiated energy is from 3.69×10^{10} to 2.59×10^{13} J, and the relationship between the seismic moment is calculated as $\log E_s = -9.70 + 1.36\log M_0$ with regression coefficient R^2=0.91.

Only three of the records were in the Harvard catalog (GCMT). To compare the moment magnitude (and the scalar momemt) obtained from the GIT with the GCMT catalog, their values are shown in Table 3. The slight difference is due to the choice of empirical relationship between Mw and M_0. In the GCMT catalog, the formula of Kanamori (1977) has been used (that is, Mw=2/3*(log M_0 – 9.1), while in this study, the formula of Hanks and Kanaamouri (1979) is considered.

5 Path

One of the results of inversion is nonparametric attenuation functions, which are estimated at different frequencies. For example, Figure 7 shows three attenuation functions at frequencies 2.75, 9.17, and 20.46. As can be seen, the attenuation function changes smoothly and decreases with increasing distance. To

Table 2. Some of the source parameters such as moment magnitude (Mw), corner frequency (fc), seismic moment (M0), source radius (r), stress drop (Δσ), apparent stress (σ_a), S-wave energy (E).

Source Number	Lon.	Lat.	Depth	ML	Mw	fc (Hz)	RMS	M0 (N.m)	r (m)	Δσ (Mpa)	σ_a (Mpa)	E (J)
1	45.865	34.466	8.0	4.00	4.29	3.11	1.19	3.05E+15	443.30	15.35	3.39	2.85E+11
2	45.803	34.605	8.0	4.50	4.60	1.79	0.96	8.91E+15	770.20	8.54	1.89	4.63E+11
3	45.804	34.421	10.0	4.80	4.74	2.4	1.55	1.45E+16	574.44	33.37	7.37	2.94E+12
4	45.824	34.428	10.0	4.30	4.50	2.76	1.24	6.31E+15	499.52	22.16	4.89	8.51E+11
5	45.755	34.421	8.0	4.70	4.85	1.83	1.87	2.11E+16	753.37	21.63	4.78	2.78E+12
6	45.74	34.471	8.0	4.50	4.63	2.69	1.18	9.89E+15	512.51	32.14	7.10	1.93E+12
7	45.911	34.457	8.0	4.10	4.29	2.76	0.63	3.05E+15	499.52	10.73	2.37	1.99E+11
8	45.849	34.504	8.0	4.00	4.11	2.41	0.17	1.64E+15	572.06	3.84	0.85	3.83E+10
9	45.588	34.589	9.5	4.20	4.48	2.91	1.49	5.89E+15	473.77	24.24	5.35	8.69E+11
10	45.615	34.403	9.3	3.80	4.02	3.24	0.27	1.20E+15	425.51	6.83	1.51	5.00E+10
11	45.558	34.598	8.0	3.80	3.94	5.14	0.46	9.12E+14	268.22	20.68	4.57	1.15E+11
12	45.631	34.512	13.0	4.50	4.57	2.49	1.02	8.04E+15	553.68	20.72	4.58	1.01E+12
13	45.96	34.447	8.0	4.10	4.35	3.06	0.7	3.76E+15	450.54	17.99	3.97	4.11E+11
14	45.951	34.426	10.0	3.90	4.14	2.57	0.51	1.82E+15	536.44	5.16	1.14	5.71E+10
15	46.392	35.218	8.5	4.20	4.07	2.61	0.34	1.43E+15	528.22	4.24	0.94	3.69E+10
16	45.832	34.901	12.0	4.30	4.57	2.56	0.84	8.04E+15	538.54	22.52	4.97	1.10E+12
17	45.653	34.554	10.0	4.00	4.17	3.21	0.48	2.02E+15	429.49	11.15	2.46	1.37E+11
18	45.693	34.758	10.0	4.20	4.46	2.61	0.83	5.50E+15	528.22	16.32	3.60	5.46E+11
19	45.832	34.578	15.0	4.40	4.47	2.22	1.09	5.69E+15	621.02	10.39	2.30	3.60E+11
20	45.81	35.105	8.0	4.80	5.07	1.5	3.91	4.52E+16	919.11	25.47	5.63	7.01E+12
21	45.64	34.64	8.0	4.70	4.67	2.23	2.2	1.14E+16	618.23	21.02	4.64	1.45E+12
22	45.938	35.1	10.0	4.30	4.59	2.26	1.11	8.61E+15	610.03	16.60	3.67	8.7E+11
23	45.733	34.428	5.8	4.20	4.39	2.21	0.46	4.32E+15	623.83	7.78	1.72	2.04E+11
24	45.75	35.07	20.0	5.30	5.39	1.11	4.19	1.36E+17	1242.04	31.17	6.88	2.59E+13
25	45.844	35.106	10.0	4.90	4.95	1.88	1.8	2.99E+16	733.33	33.13	7.32	6.02E+12
26	45.874	34.764	7.7	4.20	4.43	2.71	1.06	4.95E+15	508.73	16.47	3.64	4.97E+11
27	45.826	34.467	8.0	4.50	4.63	2.49	0.93	9.89E+15	553.68	25.49	5.63	1.53E+12
28	46.262	34.665	6.0	4.60	4.76	1.96	0.74	1.55E+16	703.40	19.48	4.30	1.84E+12
29	45.793	34.588	12.0	4.40	4.59	2.02	0.85	8.61E+15	682.51	11.85	2.62	6.21E+11
30	45.79	34.47	14.0	5.00	5.00	1.55	0.27	3.55E+16	889.46	22.07	4.87	4.77E+12

Table 3. Values of Mw and M_0 in GCMT and GIT.

Source Number	Origin Time		M0 (this study)	Mw (this study)	M0 (GCMT)	Mw (GCMT)
	yy/mm/dd	hh:mm: ss				
24	17/12/11	14:09:56	1.36×10^{17}	5.4	2.7×10^{17}	5.5
25	17/12/11	14:42:40	2.99×10^{16}	4.9	2.33×10^{16}	4.8
30	18/01/06	15:22:07	3.55×10^{16}	5.0	5.39×10^{16}	5.1

better understand the attenuation function curve, its variations in all 40 selected frequencies along with curve 1/R are shown in Figure 8. This figure is plotted in the four different displacements (less than 20 km, 20 to 35 km, 35 to 50 km, and more than 50 km). Due to the choice of R_0=9Km as the reference distance, the log (A, R) in this distance is zero. Although they all show that the attenuation increased slowly and almost uniformly with distance, the rate of attenuation increased at greater distances than at shorter distances. It should be noted that from a distance of 9 km to 45 km, which is a large number of data, we were able to divide the distance into 2 km sections (N = 18). We divided the distance greater than 45 km into 5 km sections (N= 5). That is, in total N= 23.

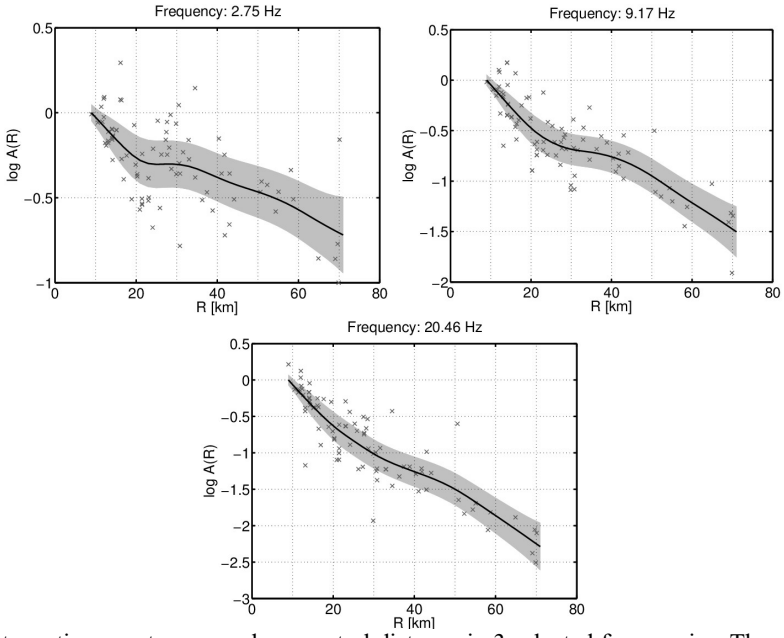

Figure 7. the attenuation spectra versus hypocentral distance in 3 selected frequencies. The gray crosses and shaded area represent the attenuation and the standard deviation around the mean, respectively.

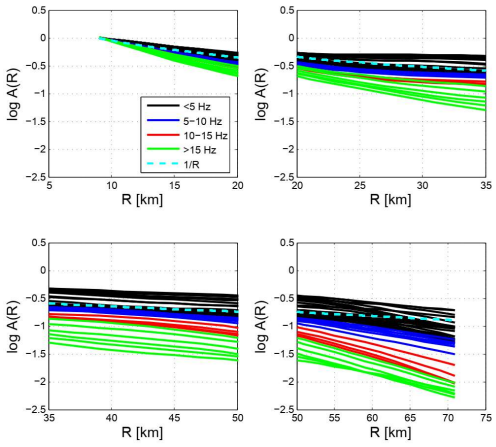

Figure 8. Attenuation spectra versus hypocentral distance for all frequencies.

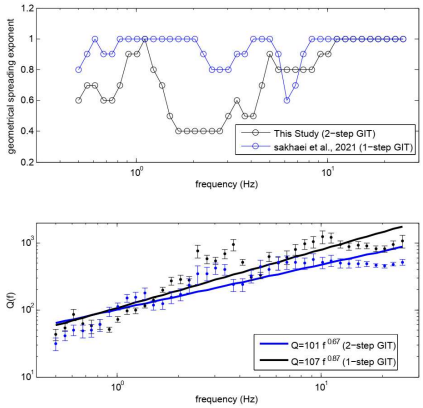

Figure 9. top The geometrical spreading exponent for all frequencies. bottom) The Q values at each frequency (0.5 to 25 Hz) along with their error bars. The solid lines represent the best fitted of Q-model for this study and previous study.

Considering the attenuation equation (Boore, 2003):

$$A(f,R) = \frac{R_0}{R^b}\exp\left(\frac{-\pi f}{Q(f)\cdot\beta}(R-R_0)\right) \quad (16)$$

In this study, $\frac{R_0}{R^b}$ is a simple model of geometrical spreading with b as a geometrical spreading coefficient. By applying the logarithm to the sides of Equation (16) and arranging its sentences we will have:

$$\log A(f,R) - \log\left(\frac{R_0}{R^b}\right) = \frac{-\pi f}{Q(f)\cdot\beta}(R-R_0) \quad (17)$$

According to the necessary condition of $\log A(f,R) - \log\left(\frac{R_0}{R^b}\right) < 0$, we seek out a maximum b to meet this condition for each frequency, indicating the strongest geometrical spreading (Wang et al., 2018). By drawing the diagram of the left of Equation (17) versus distance (for each frequency) and calculating the slope, the Q factor will be determined. On the other hand, we considered an additional condition (in addition to the above condition) so that by selecting it, the regression coefficient of Equation (17) becomes at least 0.80. Values of 0.3 to 1 were tested for all frequencies and the appropriate value is shown in Figure 9. It has also been compared with the previous study (1-step GIT). As can be seen, values of b are different in 1-step and 2-step approaches. It is clear that this difference is due to the different attenuation functions in these two approaches. Ahmadzadeh and Javan Doloei (2019) also obtained different attenuation functions for the Zagros by these two approaches, which may be due to the conditions of the sites. The temporary seismic stations located on the surface of the ground with a few meters of clay have severe amplification effects with considerable differences between site responses (Ahmadzadeh and Javan Doloei, 2019). The values of Q at different frequencies are shown in Figure 9. A line ($Q=Q_0f^N$) was traditionally fitted to it. In this study, the quality factor was estimated as $101f^{0.67}$ by the least-square solution. ,To compares the results of one-step and two-step approaches, the Q values of the previous study are also shown in this figure.

6 Site Effect

As mentioned, in order to eliminate the degree of freedom of Equation 5, the response of the one or more stations will be considered a default value. In some studies, a frequency-independent site response for very hard rock site is used (e.g. Ren et al., 2013; Wang et al., 2018). In these studies, the site response is constrained to be a specific number (usually 1 or 2) at all frequencies. In other studies, some authors also used a specific (even frequency-dependent) site response (e.g., Hassani et al., 2011; Aram and Khazaei, 2019).

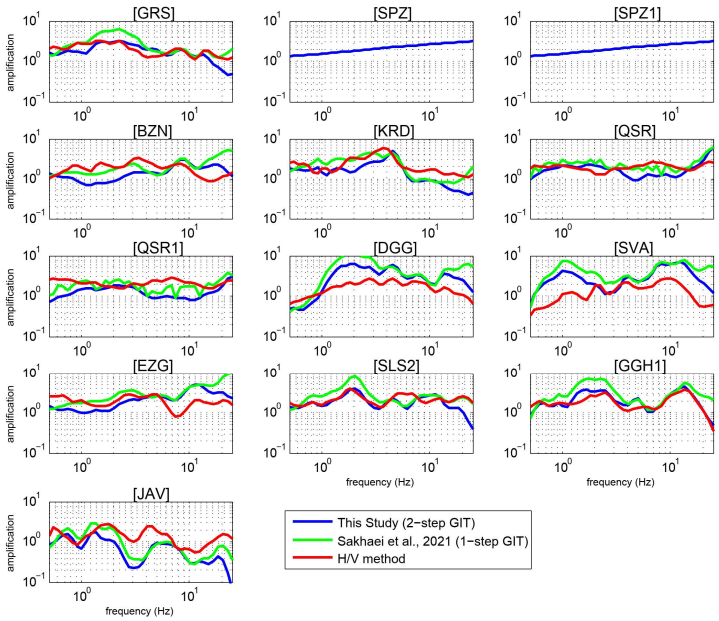

Figure 10. The site responses were obtained by GIT and H/V methods.

In this study, because the type of all sites doesn't know, the site response of previous studies has been used. Boore and Joyner (1997) estimated the site response for the site with Vs30=620 m/s. According to Table 1, among our sites, the SPZ station has Vs30=619 m/s and that is a generic rock site. Therefore, the site response of the SPZ (and SPZ1) station was assumed to be known (i.e. equal to the values obtained by Boore and Joyner (1997) for V_{s30}=620 m/s).

Lermo and Chavez-Garcia (1993) estimated the effects of the site by dividing the horizontal component of the earthquake record by its vertical component (the H/V method) and then this method has been widely used by various researchers. In this method, it is assumed that the local effects of the site do not have a significant effect on the vertical component records. In this section, the effects of the site obtained from GIT and the H/V method were compared. The diagrams of site amplification from 2-step GIT (blue line), 1-step GIT (green line), and H/V method (red line) in the frequency range of 0.5 to 25 Hz are shown in Figure 10.

7 Discussion and Conclusion

The source, attenuation, and site parameters of the 2017 Sarpol-e Zahab aftershocks were investigated using the 2-step generalized inversion method. 87 acceleration records were selected from 30 sources for inversion. In order to evaluate the accuracy of the inversion results, the residuals from the synthetic results (generated by GIT) and observations were calculated at each frequency. In this work, the residual diagrams in four frequencies of 1.23, 6.14, 10.14, and 18.50 are shown in the first row of Figure 11. This diagram is plotted in terms of hypocentral distance. In order to better represent of error bars, all the residuals of all the frequencies are plotted together as shown in Figure 11. Given the small amount of residual and also the independence of the distance, it can be concluded that the results of the inversion are reliable and close to reality.

The range of the corner frequency and the seismic moment varies from 1.11 to 5.14 Hz and from 9.12×10^{14} to 1.36×10^{17} N.m, respectively. This range is consistent with other studies. For example, Zafarani

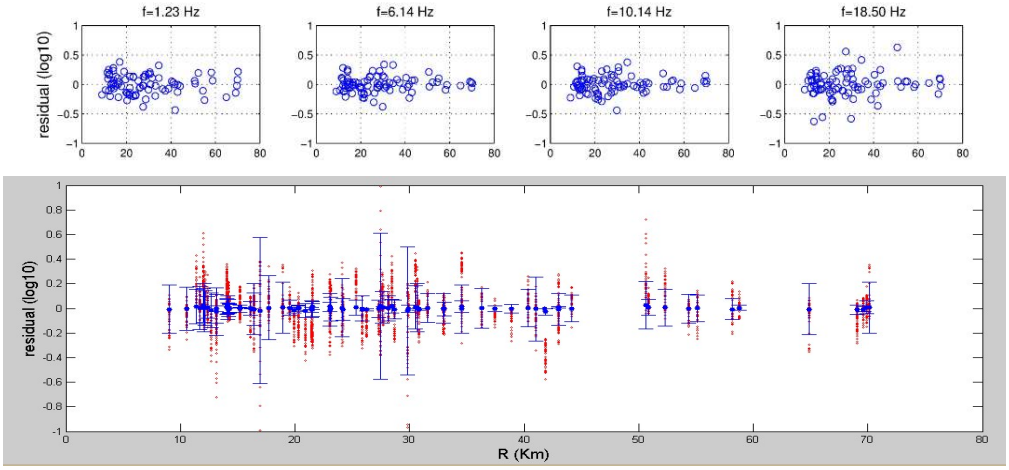

Figure 11. Top: residual diagram of GIT for all data at 4 frequencies (f=1.23 Hz (first column), f=6.14 Hz (second column), f=10.14 Hz (third column), and f=18.50 Hz (fourth column)). Bottom: all the residuals of all the frequencies together in a plot (red dot) vs the hypocentral distance and the average value (blue dot) and the corresponding standard deviation.

et al. (2012) estimated the corner frequency of Alborz as the range of 0.05 to 4 Hz. Their data ranged in moment magnitude from 4 to 7.4 and seismic moment from 1.26×10^{15} to 1.41×10^{20} N.m. Also, Wang et al. (2018) calculated the seismic moment and corner frequency for Wenchuan aftershocks from 2.0×10^{14} to 1.7×10^{18} N.m and from 0.1 to 3.1 Hz, respectively. In more recent studies, Ahmadzadeh et al. (2019) and Sakhaei et al. (2021) determined the corner frequencies in the Alborz and Zagros regions from 0.6 to 14 Hz and from 0.8 to 3.8 Hz, respectively.

In this study, we estimated $\Delta\sigma$=3.84 to 33.37 Mpa. As we mentioned: 'the stress drop $\Delta\sigma$ for small to moderate earthquakes varies from 0.1 to 100 MPa (Kanamori, 1994)'. However, in order to compare with other studies:

- Hamzehloo et al. (2010) Calculated only three events: 3.2Mpa (for Mw=5.1), 4.3Mpa (for Mw=6.1), and 2.8Mpa (for Mw=4.9).
- Zafarani and Hassani (2013): Stress drops range from 1.4 to 35.0 MPa (14 to 350 bars), with no clear dependence on magnitude.
- Ahmadzadeh et al. (2017): The estimated stress drops range from 0.04 to 5.3 MPa with an average of 0.9 MPa, within the range typically observed for crustal earthquakes in other regions of the World.
- Zafarani et al. (2012): The Brune stress drop estimates for individual earthquakes range from about 5 to 617 bars and the average value is around 135 bars for the magnitude range of events considered in this study. The estimated stress drop values are scattered and a scaling relation is not so obvious, but most of the values lie between 30 and 400 bars (for Alborz).

Therefore, despite the low differences with other studies, it is in good agreement with the results of Zafarani and Hassani (2013).

As mentioned, the relationship between moment magnitude and local magnitude is estimated as Mw=0.86ML+0.76. In order to compare this relationship with previous studies, 6 equations were considered to form table 4.

The relationship obtained in this study agrees well with other relationships, especially with the relationship of Shahvar et al. (2013), which has the least differences with it. In order to better represent and compare these relationships, their diagrams for the local magnitude range 3.6 to

Table 4. Some of the relationships between Mw and ML which considered in this paper.

Number	Equation	Region	Reference
1	Mw=0.67ML+1.62	Zagros	(Karimiparidari et al., 2013)
2	Mw=0.74ML+1.35	Zagros	(Shahvar et al., 2013)
3	Mw=0.81ML+1.10	Zagros	(Mousavi-bafrouei et al., 2014)
4	Mw=1.01ML-0.05	Zagros	(Zare et al., 2014)
5	Mw=0.68ML+0.91	Parts of Zagros	(Ahmadzadeh et al., 2017)
6	Mw=0.71ML+1.27	Parts of Zagros	(Sakhaei et al., 2021)

Table 5. Comparison between the source parameters obtained 1-step (Sakhaei et al., 2021) and 2-step (This study) GIT.

	Average		Maximum		Minimum	
Source Parameter	2-step	1-step	2-step	1-step	2-step	1-step
Corner frequency (Hz)	2.48	1.98	5.14	3.80	1.11	0.80
Seismic moment (N.m)	1.41×10^{16}	7.58×10^{15}	1.36×10^{17}	7.90×10^{16}	9.12×10^{14}	5.30×10^{14}
Stress drop (Mpa)	17.95	7.65	33.37	30.18	3.84	0.98
Moment magnitude	4.52	4.36	5.39	5.20	3.94	3.80
S-wave energy (J)	2.16×10^{12}	4.93×10^{11}	2.59×10^{13}	4.41×10^{12}	3.69×10^{10}	5.96×10^{9}

5.5 are shown in Figure 12. The quality factor calculated in this study and other studies performed for Zagros has been compared with each other. Figure 13 (right) shows four three Q diagrams from the studies of Hamzehloo et al. (2010), Ahmadzadeh et al. (2017), Sadeghi-Bagherabadi et al. (2020), and Sakhaei et al. (2021). They estimated the Q factor to be $121f^{0.55}$, $36f^{0.77}$, $141f^{0.84,}$ and $107f^{0.87}$ respectively. The Q factor obtained in this study is well consistent with other results, especially with Hamzehloo et al. (2010). The slight differences between them can be due to the choice of different frequency ranges, the choice of different geometrical spreading, as well as the use of different methods for estimating the Q factor.

In order to quantitatively compare the results of the previous study (Sakhaei et al., 2021) and the results of this study, the minimum, maximum and average values of some source parameters obtained in both 1-step and 2-step inversion are shown in Table 5. Although there is little difference between the results of these two studies and they can be considered to be consistent with each other, the values obtained in this study are more than the values obtained from the 1-step inversion. Because there is a cumulative attenuation effect on the source spectrum in the previous study. While in this study, this effect is removed from the source spectrum in the second step of inversion. In other words, the source spectrum is adjusted to its true value. Therefore, the amplitude of the source spectrum in this study is greater than its amplitude in the previous study (due to the elimination of the attenuation effect). It is clear that the source parameters mentioned in Table 5, which are directly related to the amplitude values of the source spectrum, are estimated in the previous study less than the values of the present study. As a result, it seems that in cases where R_0 is small, these differences can be ignored and similar results were obtained in both studies. But in cases where R_0 is large, we will see a significant difference and the source parameters obtained from the inversion are not reliable without removing the cumulative attenuation effect. This result can also be true for the non-parametric attenuation function (and consequently the quality factor).

We compared the site effects that were calculated by two different methods (GIT and H/V). In most cases, a very good agreement was observed and the small difference between them is mainly due to the constraints and assumptions of these

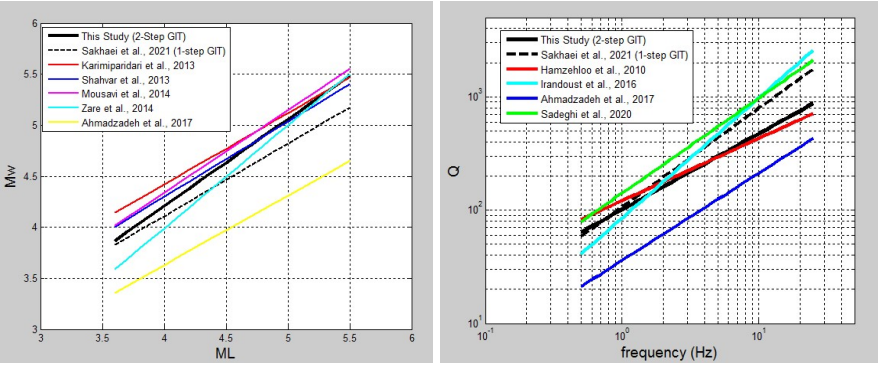

Figure 12. (Left) Comparison between the relationship between local magnitude and moment obtained in this study and other previous studies. (Right) Comparison between the quality factor obtained in this study and other previous studies.

two methods; Because in the H/V method, the site effects on the vertical component are eliminated, and on the other hand in the GIT, the site effects for the reference station (in this study SPZ and SPZ1) are default values.

Acknowledgment

We thank the Road, Housing, and Urban Development Research Center of Iran for providing accelerometric data. The authors also feel the need to thank Dr. Adrien Oth for advice and guidance on inversion codes in MATLAB software. The Authors acknowledge International Institute of Earthquake Engineering and Seismology (IIEES).

Data Availability

The data underlying this article were accessed from Road, Housing and Urban Development Research Center of Iran (https://www.bhrc.ac.ir/enismn). The Figure 1 was created using the Generic Mapping Tools v. 4.2.1 (www.soest.hawaii.edu/gmt, Wessel and Smith, 1998) and other figures were plotted by MATLAB software (https://www.mathworks.com/products/matlab.html).

References

Ahmadzadeh, S., Javan-Doloei, G., 2019, Site amplification effects on inversion results (case study: Zagros and Alborz regions), 8th international conference on seismology and earthquake engineering, Tehran, Iran

Ahmadzadeh, S., Javan-Doloei, G., Parolai, S. and Oth, A., 2019, Non-parametric spectral modelling of source parameters, path attenuation and site effects from broad-band waveforms of the Alborz earthquakes (2005–2017). *Geophys. J. Int.,* 219(3): 1514-1531.

Ahmadzadeh, S., Parolai, S., Javan-Doloei, G., Oth, A., 2017, Attenuation characteristics, source parameters and site effects from inversion of S waves of the March 31, 2006 Silakhor aftershocks. Annals of Geophysics, 60:Suppl. to 6

Andrews, D. J., 1986, Objective determination of source parameters and similarity of earthquakes of different sizes, in Earthquake Source Mechanics, edited by Das S, Boatwright J, Scholz CH, 259-268, AGU, Washington D.C

Aram, M. R., Khazaie, B., 2019, Evaluation of Strong-Motion Parameters in Qom Province in Iran Using Generalized Inversion Method. *Bulletin of Earthquake Science and Engineering*, 6 (3): 27-42

Boatwright, J., Fletcher, J., Fumal, T., 1991, A general inversion scheme for source, site, and propagation characteristics using multiply recorded sets of moderate-sized earthquakes. *Bull. seismol. Soc. Am*., 81:1764-1782

Boore, D. M., Joyner, W. B., 1997, Site

amplifications for Generic Rock Sites, *Bull. seismol. Soc. Am*., 87:327–341

Boore, D. M., 2003, Simulation of ground motion using the stochastic method. *Pure Appl. Geophys.,* 160(3):635–76

Brune, J. N., 1970, Tectonic stress and the spectra of seismic shear waves from earthquakes. *J. Geophys. Res.,* 75:4997-5009

Brune, J. N., 1971, Correction. *J. Geophys. Res.,* 76, 5002

Castro, R. R., Anderson, J. G., Singh, S. K., 1990, Site response, attenuation and source spectra of Swaves along the Guerrero, Mexico, subduction zone. *Bull. seismol. Soc. Am*., 80:1481-1503

Efron, B., 1979, Bootstrap methods, another look at the jacknife, *Ann. Stat.,* 7, 1-26.

Hamzehloo, H., Rahimi, H., Sarkar, I., Mahood, M., MirzaeiAlavijeh, H., Farzanegan, E., 2010, Modeling the strong ground motion and rupture characteristics of the March 31, 2006, Darb-e-Astane earthquake, Iran, using a hybrid of near-field SHwave and empirical Green's function method, *J. seismology*, 14:169-195

Hanks, T. C., Kanamori, H., 1979, A Moment Magnitude Scale. *J. Geophys. Res.,* 84:2348–2350

Hartzell, S. H., 1992, Site response estimation from earthquake data. *Bull. seismol. Soc. Am.,* 82:2308-2327

Hassani, B., Zafarani, H., Farjoodi, J. and Ansari, A., 2011, Estimation of site amplification, attenuation and source spectra of S-waves in the East-Central Iran. *Soil Dyn. Earthquake Eng.,* 31(10), 1397-1413.

Husid, P., 1967, Gravity effects on the earthquake response of yielding structures. Report of Earthquake Engineering Research Laboratory, California Institute of Technology, Pasadena, California

Izutani, Y., Kanamori, H., 2001, Scale dependence of seismic energy-to-moment ratio for strike-slip earthquakes in Japan. *Geophys. Res. Letters*, 28:4007–4010

Jackson, J. A., McKenzie, D. P., 1984, Active tectonics of the Alpine-Himalayan belt between Western Turkey and Pakistan. *Geophys. J. Roy. Astron. Soc*., 77(1):185–264

Kanamori, H. (1977). The energy release in great earthquakes. *J. Geophys. Res.*, 82:2981-2987

Kanamori, H., 1994, Mechanics of earthquakes, *Annu. Rev. Earth Planet. Sci.,* 22:207–237

Karimiparidari, S., Zaré, M., Memarian, H., Kijko, A., 2013, Iranian earthquakes, a uniform catalog with moment magnitudes. *J. Seismology,* 17(3):897-911

Kinoshita, S. H., 1994, Frequency-Dependent Attenuation of Shear Waves in the Crust of the Southern Kanto Area, Japan. *Bull. seismol. Soc. Am*., 84:1387-1396

Konno, K., Ohmachi, T., 1998, Ground-motion characteristics estimated from spectral ratio between horizontal and vertical components of microtremor. *Bull. seismol. Soc. Am.,* 88:228–241

Lermo, J., Chavez-Garcia, F., 1993, Site effect evaluation using spectral ratios with only one station. *Bull. seismol. Soc. Am.,* 83:1574–94

Mousavi-bafrouei, S. H., Mirzaei, N., Shabani, E., 2014, A Declustered Earthquake Catalog for the Iranian Plateau. *Annals of Geophysics,* 57(6):1-25

Motaghi, K., Shabanian, E., Kalvandi, F., 2017, Underplating along the northern portion of the Zagros suture zone, Iran. *Geophys. J. Int.,* 210:375-389

Nemati, M., Tatar, M., 2015, Relations between source parameters for large Persian earthquakes. *Annals of Geophysics,* 58(5):S0543

Nissen, E., Tatar, M., Jackson, J. A, Allen, M. B., 2011, New views on earthquake faulting in the Zagros fold-and-thrust

belt of Iran. *Geophys. J. Int.,* 186(3):928–944

Oth, A., 2007, Source Processes and Spectral Ground Motion Models of Intermediate-Depth Vrancea (Romania) Earthquakes, Ph.D. thesis, Universität Karlsruhe (TH)

Oth, A., Bindi, D., Parolai, S., Wenzel, F., 2008, S-Wave attenuation characteristics beneath the Veranca region in Romania: new insights from the inversion of ground-motion spectra. *Bull. seismol. Soc. Am.,* 98:2482–2497

Oth, A., Parolai, S., Bindi, D., Wenzel, F., 2009, Source spectra and site response from Swaves of intermediate-depth Vrancea, Romania, earthquakes, *Bull. Seismol. Soc. Am.,* 99:235 254

Parolai, S., Bindi, D., Augliera, P., 2000, Application of the generalized inversion technique (GIT) to a microzonation study: numerical simulations and comparison with different site-estimation techniques. *Bull. seismol. Soc. Am.,* 90:286-297

Parolai, S., Bindi, D., Baumbach, M., Grosser, H., Milkereit, C., karakisa, S. and Zunbul, S., 2004, Comparison of different site response estimation techniques using aftershocks of the 1999 Izmit earthquake, *Bull. Seism. Soc. Am.*, 94:1096-1108

Paul, A., Kaviani, A., Hatzfeld, D., Vergne, J., Mokhtari, M., 2006, Seismological evidence for crustal scale thrusting in the Zagros mountain belt (Iran), *Geophys. J. Int.,* 166(1):227–237

Ren, Y. F., Wen, R. Z., Yamanaka, H. and Kashima, T., 2013, Site effects by generalized inversion technique using strong motion recordings of the 2008 Wenchuan earthquake, *Earthquake Eng. Eng. Vibr.,* 12, 165–184.

Sakhaei, S. R., Mahood, M., Heidari, R., Arian, M., 2021, Determination of Source, Site, and Path Effects of Mw = 7.3, 2017 Sarpol-e Zahab Using a Non-Parametric Generalized Inversion Technique. *Pure Appl. Geophys.,* https://doi.org/10.1007/s00024-021-02881-1

Sadeghi-Bagherabadi, A., Sobouti, F., Pachhai, S., Aoudia, A., 2020, Estimation of geometrical spreading, quality factor and kappa in the Zagros region. *Soil Dyn. Earthquake Eng.,* 133: p.106110

Salazar, W., Sardina, V., Cortina, J., 2007, A hybrid inversion technique for the evaluation of source, path, and site effects employing S-wave spectra for subduction and upper-crustal earthquakes in El Salvador. *Bull. seismol. Soc. Am.,* 97:208-221

Shahvar, M. P, Zare, M., Castellaro, S., 2013, A unified seismic catalog for the Iranian plateau (1900-2011), *Seismol. Res. Lett.,* 84:233-249

Tatar, M., Hatzfeld, D., Ghafori-Ashtiany, M., 2004, Tectonics of the Central Zagros (Iran) deduced from microearthquake seismicity, *Geophys. J. Int.,*156:255–266

Wang, H., Ren, Y., Wen, R., 2018, Source parameters, path attenuation and site effects from strong-motion recordings of the Wenchuan aftershocks (2008–2013) using a non-parametric generalized inversion technique. *Geophys. J. Int.,* 212:872–890

Wessel, P., Smith, H. F., 1998, New, improved version of generic mapping tools released. *Earth Space Sci.,* News, 79. Doi: 10.1029/98EO00426

Zafarani, H., Hassani, B., Ansari, A., 2012, Estimation of earthquake parameters in the Alborz seismic zone, Iran using generalized inversion method. *Soil Dyn. Earthquake Eng.,* 42:197-218

Zafarani, H. and Hassani, B., 2013. Site response and source spectra of S waves in the Zagros region, Iran. *J. seismology*, 17: 645-666

Zare, M., Amini, H., Yazdi, P., Sesetyan, K., Demircioglu, M. B, kalafat, D., Erdik, M., Giardini, D., Asifkhan, M.,

Tsereteli, N., 2014, Recent developments of the Middle East catalog, *J. Seismology,* 18:749-772